2020-01-01

3D Printed Alginate-Based Zinc Oxide Nanoparticle Scaffolds For Wound Healing

Carol Cleetus
University of Texas at El Paso

Recommended Citation

Cleetus, Carol, "3D Printed Alginate-Based Zinc Oxide Nanoparticle Scaffolds For Wound Healing" (2020). *Open Access Theses & Dissertations*. 2950.
https://scholarworks.utep.edu/open_etd/2950

3D PRINTED ALGINATE-BASED ZINC OXIDE NANOPARTICLE SCAFFOLDS FOR WOUND HEALING

CAROL M. CLEETUS

Master's Program in Biomedical Engineering

APPROVED:

Binata Joddar, Ph.D., Chair

Charles T. Spencer, Ph.D.

David Roberson, Ph.D.

Stephen L. Crites, Jr., Ph.D.
Dean of the Graduate School

Dedication

I dedicate this research to my parents and sister, whose constant support, prayers, and guidance have gotten me through each and every step in my life. I also dedicate this to my uncle Justin who encouraged my every academic endeavor.

3D PRINTED ALGINATE-BASED ZINC OXIDE NANOPARTICLE SCAFFOLDS FOR WOUND HEALING

by

CAROL M. CLEETUS, B.S.

THESIS

Presented to the Faculty of the Graduate School of
The University of Texas at El Paso
in Partial Fulfillment
of the Requirements
for the Degree of

MASTER OF SCIENCE

Department of Metallurgical, Materials, and Biomedical Engineering
THE UNIVERSITY OF TEXAS AT EL PASO
May 2020

Acknowledgements

First, I would like to thank my thesis advisor and committee chair, Dr. Binata Joddar, for her guidance and mentorship. I am grateful for her invaluable training over the last two years.

I would also like to thank the number of faculty members who have helped me along the way, including Dr. Juan Noveron who conceived the idea for this research and Dr. Charles Spencer for his assistance in its execution and serving on my defense committee. I also thank Dr. David Roberson for agreeing to be a member of my committee.

I would like to acknowledge the members of the MMBME department who have assisted me, especially Dr. Thomas Boland for his continued guidance and advice throughout this program.

I thank Igor Estevao for his assistance and patience during numerous training sessions in the BBRC.

Finally, I would like to extend my gratitude to my labmates in IMSTEL, who have made this entire experience more enjoyable. A special thanks to Gisel Fregoso for the countless early mornings and weekends that made this research possible.

Abstract

Effective treatment of chronic wounds is essential for the prevention of infection and scar tissue formation, requiring a novel approach to address the limitations of existing options. This study utilizes Calcium Chloride ($CaCl_2$) crosslinked alginate, a common biomaterial widely used in wound dressing, and UV activated Zinc Oxide (ZnO) nanoparticles (NPs) for their potential hydroxyl radical mediated antibacterial applications. ZnO NPs were synthesized by combustion method from Zinc Nitrate Hexahydrate and Sucrose. Scanning Electron Microscopy (SEM) and X-Ray Diffraction (XRD) characterization were used to verify composition and NP size. Terephthalic Acid, used as a fluorescent probe, confirmed the generation of hydroxyl radicals from the NPs. 3D printed lattice structures and manually cast structures were studied to compare the mechanical properties and benefits of each. Swelling and degradation assays, as well as SEM imaging revealed the greater structural integrity of the 3D printed structures, with an increased porosity having potential to facilitate molecular exchange. In addition, the 3D printed ZnO NP laden alginate scaffolds indicated increased moisture retention when compared to alginate only structures using a humidity monitoring system. Antibacterial testing on *Staphylococcus epidermidis* (*S. epidermidis)* suggests that both 0.5% and 1% ZnO concentrations have antibacterial properties comparable to the commercially available antibiotic Erythromycin, while a Live/Dead assay confirmed viability of fibroblasts on the scaffolds. Overall, this study explores and validates the potential to develop a customizable, biocompatible, and antibacterial wound healing patch.

Table of Contents

List of Tables

List of Figures

Chapter 1: Introduction

1.1 Biomaterials

Biomaterials can be defined as natural or synthetic materials which can interface with biological systems. They can be utilized in tissue engineering to repair, replace, or influence biological processes with a goal of regeneration. A major requirement of biomaterials is biocompatibility in order to ensure the lack of an inflammatory response which could lead to reduced healing or the body's rejection of the material [1].

1.1.1 Hydrogels

Hydrogels are common biomaterials characterized as 3D, crosslinked polymer networks. They are known by their high water content and have diverse physical properties, allowing them to be cast into almost any form and absorb thousands of times their weight, making them popular in medicine [2]. Their biomimicry of tissues and possession of versatile characteristics like porosity and the ability to adhere cells makes them convenient for tissue engineering study [3].

1.2 Clinical Background

Chronic wounds are identified as not being able to proceed through the natural stages of wound healing, leading them to enter a state of inflammation that delays the healing process and produces structurally compromised skin tissue. These wounds are commonly found in diabetic patients and can be attributed to the high blood sugar levels that are found within these individuals. These high levels increase inflammation and prevent nutrients from being properly delivered to cells to provide the energy required for wound healing [4]. Additionally, the skin requires water to remain structurally healthy and functional, but is unable to obtain it due to glucose increasing the thickness of blood and blood vessels narrowing due to peripheral vascular disease [5]. Such an environment is a haven for bacterial growth, not only obstructing the skin's ability to heal but worsening the tissue in such vulnerable conditions [6]. Thus, therapy directed at chronic infections could reduce the progression of diabetic wounds and other related chronic wounds.

Wound healing can usually be divided into stages as seen in Figure 1.1. The first to occur is hemostasis (or bleeding phase), in which there occurs a fibrin plug and coagulation of blood at the wound site. This is followed by the inflammatory step in which there is a debridement, along with the recruitment of fibroblasts. In the third stage, proliferative, a proliferation of fibroblasts takes place, along with stimulation of new blood vessels. The fourth and final phase is remodeling. This culminates in healing of the epidermis and dermis layers over the course of a few days or weeks [5,6]. Chronic wounds, however, involve greater tissue damage leading to delayed healing and possible formation of scar tissue after a state of continuous inflammation and injury [7].

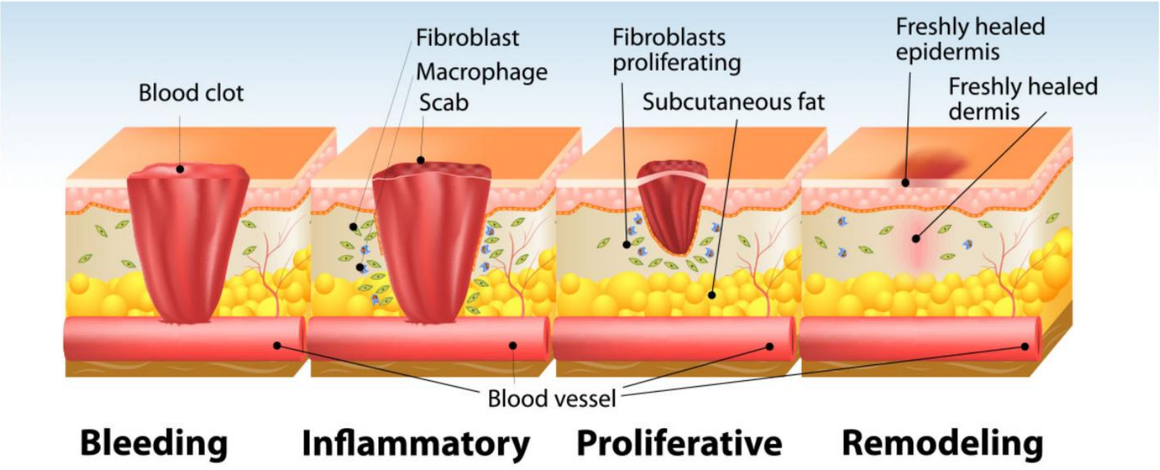

Figure 1.1: The four stages of wound healing, 1) Hemostasis, 2) Inflammation, 3) Proliferative, 4) Remodeling [5].

In order to properly address wound healing, it is necessary to develop a product to facilitate healing, acknowledging the advantages of existing treatments while combating their limitations. Some solutions may have poor wound re-epithelialization, fluid loss control, or functionality, while other therapies may extensively utilize antimicrobials which lead to antibiotic resistance [8]. Hydration is particularly essential in normal biological functions and wounds, allowing for faster healing and re-epithelialization with cell proliferation and retention of growth factors as well as lower chance of infection. Added benefits are reduced scarring and pain perception. Figure 1.2 depicts the benefits of a hydrated environment for wounds [9].

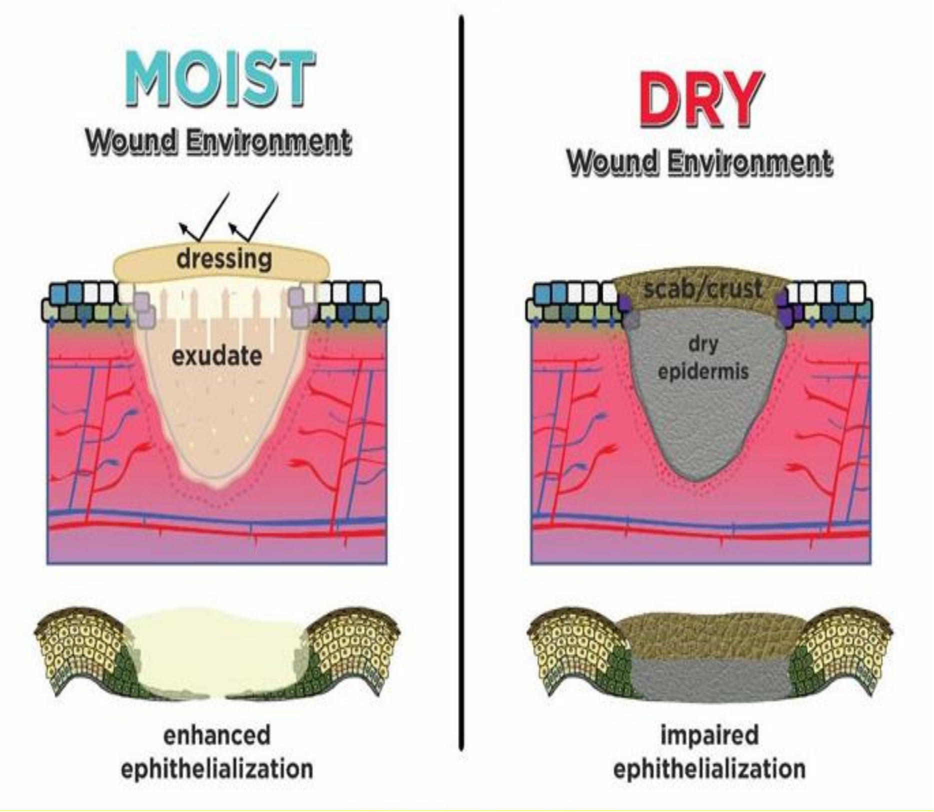

Figure 1.2: Comparison of a moist/hydrated and dry wound healing conditions [9].

1.2.1 Alginate Hydrogels for Wound Healing

Hydrogels meet some of these needs and are conducive to healing with their matrices trapping water to create a moist environment while still allowing gas diffusion. One such hydrogel is alginic acid (alginate). Alginate based wound care has emerged in numerous studies and in the commercial market indicating their appropriateness for use in wound management [7]. Properties such as biocompatibility, ability to retain moisture and reduce infection make alginate suitable for these applications. Alginate is also readily available, being derived from brown algae [10]. These intrinsic beneficial properties of alginate can be exploited in combination with those of metal oxides to provide an even more advantageous wound healing scaffold.

1.2.2 Metal Oxide NPs for Wound Healing

Nanomaterials are materials of less than 100 nm in size. Metallic NPs such as ZnO NPs are being increasingly studied and employed for wound healing applications (Table 1.1) as reports have shown them to be some of the most antibacterial inorganic materials [8].

Table 1.1: Nanoparticles and their properties for wound healing [8].

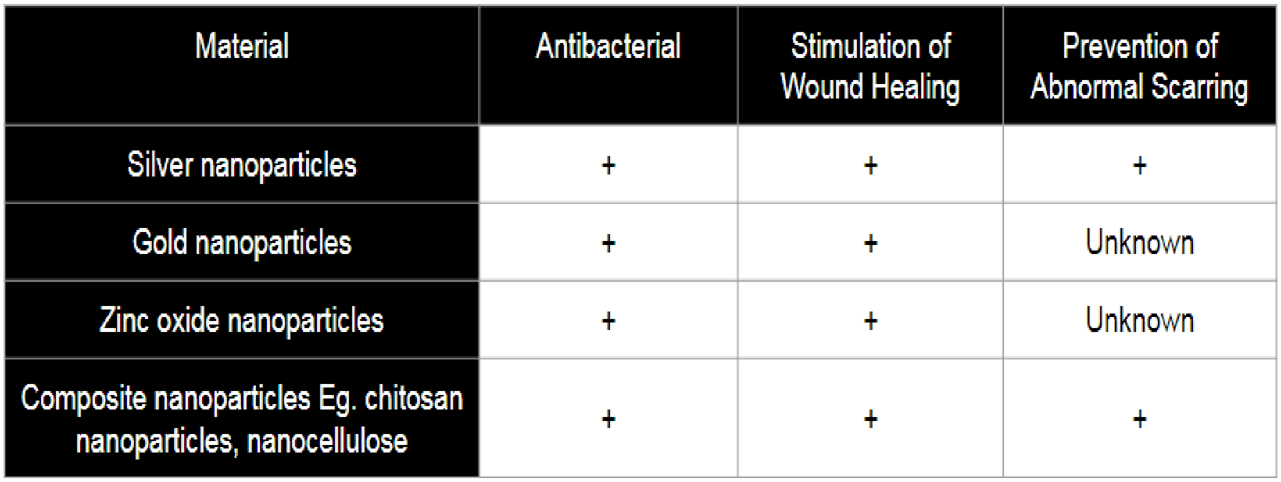

Material	Antibacterial	Stimulation of Wound Healing	Prevention of Abnormal Scarring
Silver nanoparticles	+	+	+
Gold nanoparticles	+	+	Unknown
Zinc oxide nanoparticles	+	+	Unknown
Composite nanoparticles Eg. chitosan nanoparticles, nanocellulose	+	+	+

Metal oxide NPs antibacterial mechanism is thought to be size dependent, based on NP diffusion through the cell membrane to cause damage to DNA (Figure 1.3) [11]. These NPs also show generation of reactive oxygen species (ROS) such as hydroxyl radicals under UV photocatalysis, which in turn can cause cell death [11,12]. For this study we decided to explore these characteristics in a cheap, easy to manufacture ZnO NP, while using another metal oxide, commercially obtained TiO_2, as a control.

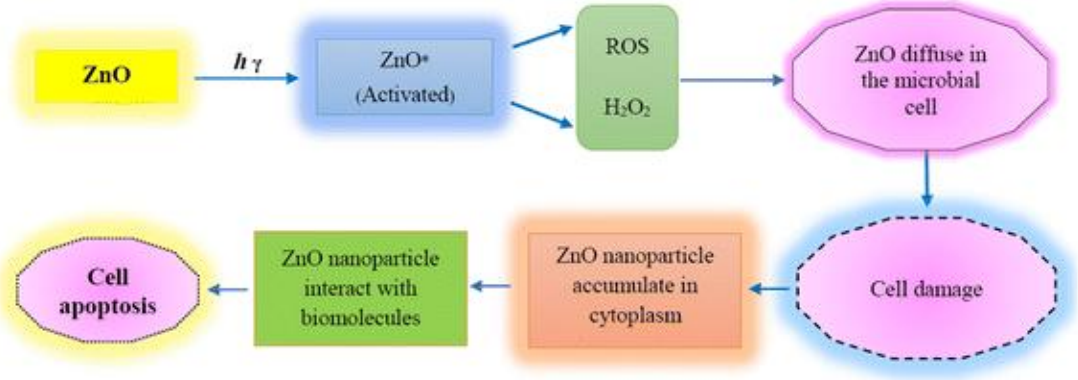

Figure 1.3: Antibacterial mechanism of ZnO NPs, depicting ROS production under UV light and NP diffusion [11].

1.3 3D Printing

Three-dimensional (3D) printing in the field of biomedical engineering has become incredibly useful and rather common, encompassing a variety of printing technologies or methods. One such method is extrusion printing, widely used in tissue engineering for the production of devices and scaffolds. This can be defined as the extrusion or dispensing of material also known an “ink” through a nozzle, often from a syringe [13].

In extrusion printing, filaments of ink are deposited layer by layer as determined by a computer model pattern. As such, an extruded object requires support to maintain its structure and prevent collapse. This can be achieved through thixotropy, temperature control, or crosslinking. In this study, we use a two-step chemical crosslinking mechanism to manipulate the alginate for both optimal extrusion and maintenance of postextrusion structure [14].

Structural fidelity can additionally be affected by the design of 3D printed structure. Based on previous study of 3D designs in our lab, a lattice structure was chosen as the prime model for this experiment due to its proven superiority [15].

1.3.1 Bioink Formulation

Although there exists many potential biomaterials, the successful development of a bioink for 3D printing remains a challenge in some cases. Printable biomaterials must generally meet certain requirements including but not limited to printability, biocompatibility, and possession of appropriate mechanical properties [14].

1.4 Hypothesis

Despite the number of wound healing therapies in existence, there remain limitations such as infection, scar tissue formation, and biofilm formation in the case of chronic wounds. Antibacterial drug resistance continues to be a growing cause for restraints in therapy [8]. Alternatives to antibiotics have yet to be fully explored. The use of a uniquely synthesized alginate – ZnO NP wound healing template can address these issues.

1.5 Objective

The need for better options on the market for chronic wound healing continues. Both alginate and ZnO NPs individually have properties making them appropriate for these applications. Research will be conducted to validate the potential for a chronic wound healing treatment composed of these materials. The morphological and mechanical properties of this system are to be validated in multiple studies. The structural strength and integrity over time will be assessed, along with the hydration retention abilities. The demonstration of antibacterial properties and fibroblast compatibility will further support these attempts and allow for comprehension of the effects of varying concentrations of ZnO NPs. Overall, this work seeks to present an alginate-ZnO gel system, suitable for 3D printing to allow for customizability, reproducibility, and efficiency in cost effective patient wound healing therapy.

Chapter 2: Materials and Methods

2.1 Materials

The Sucrose ($C_{12}H_{22}O_{11}$) and Zinc Nitrate Hexahydrate ($Zn(NO_3)_2•6H_2O$) used for the synthesis of ZnO NPs were obtained from Sigma- Aldrich Inc (St. Louis, MO). Medium Viscosity Alginic Acid Sodium Salt ($((C_6H_7O_7)A(C_6H_7O_7)BNa)$) (alginate), Calcium Chloride Dihydrate ($CaCl•2H_2O$), Phosphate Buffered Saline (PBS,10X), Sodium Hydroxide (NaOH) and Terephthalic Acid ($C_8H_6O_4$) were all procured from Thermofisher Scientific (Waltham, MA).

For bacterial testing, Blood Agar (TSA w/ 5% Sheep Blood) plates, *Escherichia coli* pellets, and *Staphylococcus aureus* KwikStik were also purchased from Thermofisher Sceintific and Erythromycin Antibiotic Sensitivity Disks from Carolina Biological Supply (Burlington, NC).

For cell culture, mitomycin-C treated STO (MITC-STO) fibroblast cells and 1% Penicillin-Streptomycin were obtained from Millipore Sigma (Burlington, MA), Fetal Bovine Serum (FBS) form Thermofisher Scientific, Dulbecco’s Modified Eagle’s Medium (DMEM)/ Nutrient Mixture F-12 Ham with 15 mM HEPES from ATCC (Manassas, VA). A LIVE/DEAD® Viability/Cytotoxicity Kit for mammalian cells was bought from Molecular Probes (Eugene, OR).

2.2 Zinc Oxide Nanoparticles Synthesis and Characterization

The ZnO NPs used in this study were synthesized by combustion method by heating Zinc Nitrate Hexahydrate ($Zn(NO_3)_2•6H_2O$) and Sucrose ($C_{12}H_{22}O_{11}$) on a hot plate [16]. To determine and confirm NP size and composition, SEM and XRD characterization were conducted on the synthesized NPs using published protocol [17]. A terephthalic acid assay was used to assess their hydroxyl radical generation capabilities [16]. In addition, each of these tests were also done on commercially obtained TiO_2 NPs to characterize this as a control for the ZnO NPs.

2.2.1 SEM

SEM (Hitachi 4800) in the secondary electron scattering mode was used to analyze the microstructure of the NPs. To avoid charging effect, the samples were sputter-coated with gold, prior to imaging. Size of the NPs was measured using ImageJ software.

2.2.2 XRD

The phase and crystal structure of the NPs were analyzed using the Rigaku Benchtop powder X-ray diffractometer (Mini Flex II) using Cu-Kα radiation (l=1.5418 Å) at room temperature. For all measurements the scan was carried out over an interval of 20°– 80° (2-7 range), step size of 0.02°, and a scan rate of 0.6°/min.. To determine the crystallite size the Debye Scherrer Relation was used. The equation is given as:

$$D = (0.9\lambda)/(\beta \cos\theta) \text{ ---------- } (1)$$

where D is the crystallite size, λ (CuKα) – 1.5406 Å, β is the full width at half maximum and θ is the diffraction angle.

2.2.3 Radical Generation Probe Test

Sodium chloride (NaCl) and terephthalic acid ($C_8H_6O_4$) were combined stoichiometrically to prepare a $5x10^{-3}$ M concentration Sodium Terephthalate (NaTA) solution. 5mg each of either ZnO or TiO_2 NPs were placed in wells with 1 mL of NaTa and placed on a belly dancer (IBI Scientific, Dubuque, IA, USA) for 10 minutes to react. The well plate was then placed under a UV bulb (Uvitron UVA 600-Watt Halide Lamp, 365 nm) in the Intelliray 600 UV chamber (Uvitron Intelliray 600 Curing Unit, West Springfield, MA) for 5 min at 100% intensity for photocatalytic hydroxyl radical release. A fluorescent probe, 2-hydroxy terephthalate, was formed by the reaction of NaTa and hydroxyl radicals, allowing for detection of the hydroxyl radicals [16,18]. Black, clear-bottom 96 well microplates (Corning Inc., Corning NY) holding 100 µL samples were read in a Fluoroskan™ Microplate Fluorometer with Ascent™ Software (Thermo Scientific) at 355 nm excitation and 444 nm emission wavelengths.

2.3 Scaffold Fabrication

2.3.1 Gel Preparation

In this study, four different alginate - NP concentrations (w/v) were used to determine any thresholds or changes in effect. These groups were alginate only, alginate + 0.5% w/v ZnO, alginate + 1% w/v ZnO, and alginate +1% w/v TiO_2. To prepare the gels, a solution of 0.25 M Calcium Chloride ($CaCl_2$) crosslinker was made first by combining 254 mg of $CaCl_2$ Dihydrate in 8 mL of deionized (DI) water. The components listed in Table 2.1 were then used to prepare the alginate-NP gel solution in 50 mL centrifuge tubes. To maintain structural fidelity for enhanced printability, the alginate was partially crosslinked by adding 100 µL of crosslinker per mL of DI water along with the corresponding ZnO or TiO_2 NPs and alginate for each solution. Immediately upon addition of alginate, the solution was vortexed to form a homogeneous mixture. The gel mixtures were then loaded in 10 mL syringes (ThermoFisher Sci.) for 3D bioprinting or manual casting, as necessary. These doses were determined based on guidance from other published works, in which a range of ZnO NPs (0.05%-1% w/w) was evaluated and displayed promising antimicrobial effects [19,20].

Table 2.1: Measured amounts of DI H_2O, 0.25 M $CaCl_2$, ZnO, TiO_2, and alginate constituting the formation of each gel sample, alginate, alginate + 0.5% ZnO, alginate + 1% ZnO, and alginate + 1% TiO_2.

Sample	DI H_2O (mL)	0.25 M $CaCl_2$ (µL)	ZnO NPs (g)	TiO_2 NPs (g)	Alginate (g)
Alginate only	4.8	500	0	0	0.2
Alginate + 0.5% ZnO	4.775	500	0.05	0	0.2
Alginate + 1% ZnO	4.75	500	0.1	0	0.2
Alginate + 1% TiO_2	4.75	500	0	0.1	0.2

2.3.2 3D Printed Gels

The syringes were fitted with 24-gauge steel tip needles (HUAHA, Amazon) and placed in a 3D extrusion bioprinter (BioBot 1, Allevi, PA, USA; Cellink, MA, USA). SolidWorks was used to design lattice cube and lattice cylinder STL files, which were modified and converted to g-code using Repetier Host software, as needed for each experiment. 20-30 psi pressure was used to print 3D lattice structures onto petri dishes, where they underwent a secondary crosslinking with 100 µL of 0.25 M $CaCl_2$ for 20 minutes, followed by a PBS wash to remove any $CaCl_2$ residue.

2.3.3 Manually Cast Gels

For cast gels, molds of 10 mm diameter and 2 mm depth were created according to silicone putty product package instructions (EasyMold® Silicone Putty, Castin' Craft®). The gels were manually extruded through the 10 mL syringes into the molds. Once cast, they were again crosslinked in 100 µL of 0.25 M $CaCl_2$ for 25 minutes and washed with PBS.

2.4 SEM of Scaffolds

A comparison of the measurements of each pore within the 3D printed and manually cast gels was obtained with cross-sectional images via SEM, as described in previously published studies [21]. Samples were crosslinked, placed in -80°C overnight, lyophilized, and sliced to reveal a cross-sectional area. These sections were sputter-coated (Gatan Model 682 Precision etching coating system, Pleasantown, CA, USA) with gold to avoid charging of particles and were then viewed through the use of SEM (S-4800, Hitachi, Japan). Analysis of each sample's average pore diameter was performed through the Image J software.

2.5 XRD of Scaffolds

Gels were cast and crosslinked before drying at room temperature overnight. They were then pulverized to powder and analyzed as described earlier by Rigaku Benchtop powder X-ray diffractometer (Mini Flex II) with Cu-Kα radiation (l=1.5418 Å) at room temperature. Scan carried out over an interval of 20°– 80° (2-7 range), with step size of 0.02°, and a scan rate of 0.6°/min.

2.6 Swelling Assay

A swelling assay was conducted to analyze the swelling capacity of both the 3D printed and manually cast gels [15]. The structures were crosslinked and placed in a desiccator to dry. After 18 hr the samples were removed, weighed to find their dry weight (W_0), and placed in PBS to swell. For the following 5 days, the samples were weighed (W_t) every 24 hr to track their solvent uptake. The swelling ratio was then calculated using the following formula for degree of swelling (Ds):

$$Ds = (W_t - W_0)/W_0 \text{ ---------- } (2)$$

2.7 Degradation

The bioprinted gels were additionally tracked over time to ascertain their physical integrity and stability. Printed cylindrical disks of 6 mm diameter were placed in a well plate and submerged in 500 µL of PBS. The gels were imaged every 24 hr over a period of 28 days.

2.8 Rheology

Rheological parameters of both the 3D printed and cast gels were analyzed via shear rheometry. 8 mm diameter disks of 1 mm height were obtained by biopsy punch and placed in 1X PBS to swell to equilibrium. An AntonPaar MCR 101 rheometer (Anton-Paar, Graz, Austria) with an 8-mm parallel plate geometry was used to conduct oscillatory shear stress analysis at 1% linear viscoelastic strain (LVE) strain from 0.05-50 Hz. All moduli, along with complex viscosity, are reported at 1.99 Hz.

2.9 Humidity Sensor

A system composed of an ELEGOO Uno R3 Board ATMega328P ATMEGA16U2 microcontroller, DHT 11 humidity and temperature sensor module, Adafruit MicroSD card breakout board, and a LCD screen was set up to monitor moisture retention of the hydrogels. Arduino software was used to program the system to take DHT11 module readings every 30 minutes and log them onto the SD card. To minimize outside air exposure, an isolated environment was created by enclosing the sensor in a 35 mm petri dish. To match the dimensions of the DHT11 humidity sensor, a 16 mm x 12 mm lattice sheet was printed for each gel type and placed atop the sensor in the petri dish. The gel was further protected from exposure by wrapping the dish in parafilm. The microcontroller was then connected and humidity and temperature readings were measured and displayed on the LCD screen. The following equation was used to evaluate the data based on relative humidity (RH) percentage recorded on the DHT11 module:

$$RH(\%) = (Density\ of\ water\ vapor/Density\ of\ water\ vapor\ at\ saturation)\ x\ 100\% \text{ ---------- } (3)$$

Each hydrogel was monitored for 6 days. This study was conducted twice (n=2).

2.10 Antibacterial Testing

Two forms of bacterial testing were conducted to assess the antibacterial properties of the NP laden gels. Erythromycin disks were used as a control to compare the antibacterial properties of the gels to a widely used and effective antibiotic. *Staphylococcus aureus* (*S. aureus*), *S. epidermidis*, and *Escherichia coli* (*E. coli*), were used to look at effectiveness on common gram positive versus gram negative bacteria. All gels were autoclaved prior to being printed into 6 mm disks and crosslinked with sterile filtered $CaCl_2$.

2.10.1 Bacterial Plate Disk Diffusion

The first test was modeled after the Kirby Bauer disk diffusion susceptibility test. The printed disks were placed in a well plate and exposed to UV for 5 minutes at 100% intensity in the Intelliray 600. TSA Blood agar plates were spread with either *E. coli* (pellet) or *S. aureus* (kwikstik). The gels were then placed on the agar plates so that each bacterial plate held one of each of the samples in a quadrant. The erythromycin disks were placed in the center of each plate. The plates were then placed in an incubator at 37°C. After 24 hours their disk diffusion was noted by measuring the diameter of the clearance zone around each disk.

2.10.2 Bacterial Broth Optical Density

Further antibacterial testing was done with a bacterial broth test on *S. epidermidis,* cultured in house, comparing UV exposed and unexposed gels. All printed gels were placed in 48 well microplates (Corning Inc., Corning NY) with 200 μL of nutrient broth pipetted into each of the wells. One erythromycin disk placed within a well served as a control in each group. One plate was placed in the Intelliray 600 for 5 minutes at 100% intensity for UV exposure, while the other plate was maintained in ambient light. To dilute the *S. epidermidis*, an inoculation loop was used to transfer 10 µL of bacteria into 5 mL of nutrient broth. 400 µL of the bacterial broth was then added to each well and the plates were incubated at 37°C for 24 hr. 100 µL of supernatant from each sample was transferred to a clear 96 well plate (Corning Inc., Corning NY) at 24 hr and 48 hr intervals after the initial incubation. The Molecular Devices VersaMax UV/Vis plate reader with VersaMax SoftMax Pro® software (Molecular Devices, LLC. San Jose, CA) was used to measure the optical density of the samples at 600 nm wavelength. This experiment was repeated twice (n=2).

2.11 Cytocompatibility

To ensure cytocompatibility of the gels, MITC-STO fibroblast cells were cultured in complete growth medium (CGM; DMEM/ Nutrient Mixture F-12 Ham with 15 mM HEPES), with 12.5% fetal bovine serum and 1% penicillin-streptomycin added. Fibroblast cells were seeded at a density of 2×10^5 cells/mL within a sterile 48-well plate. Autoclaved gels and sterile filtered $CaCl_2$ were used to 3D print disks. These samples were placed in a 48-well microplate with 200 µL DMEM and underwent 5 minutes of UV irradiation in the IntelliRay 600. The samples were then transferred to their respective wells in the sterile well plate containing cells. The plate included a control group with only cells, no gel samples, to observe general fibroblast proliferation. To each well, 200 µL of DMEM was added, and the plate was incubated for 24 hr (37°C, 5% CO_2). A LIVE/DEAD (LIVE/DEAD® Viability/Cytotoxicity Kit for mammalian cells, Molecular Probes) assay was done to confirm cell viability. Imaging (ZEISS AxioPhot Fluorescent Microscope, Germany) was performed to show the retention of viable (Calcein AM stained) cells and the presence of dead (Ethidium Homodimer-1 stained) cells in each sample.

Images were collected using ZEN digital imaging software and further analyzed through an Image J digital imaging extension, FIJI. Particle analysis was done on masked images of Calcein AM (green threshold) and Ethidium Homodimer-1 (red threshold) to measure the cells observed in the respective wells of each gel group. The equation used to obtain the percentage of live or dead cells is given as:

$$Number\ of\ Live\ or\ Dead\ Cells\ (\%) = (Number\ of\ particles\ in\ green\ or\ red\ threshold\ image/\ Total\ number\ of\ particles\ in\ green\ and\ red\ threshold\ images)\ x\ 100\ \%\ \text{-------(4)}$$

This was determined from the average particle count of each sample (n = 2)

2.12 Statistical Analysis

All experiments were performed with sample groups of at least three repeats (n=3) unless otherwise mentioned. Data are presented as the mean ± standard deviation (SD). Two-way ANOVA, followed by Tukey post-test for multiple comparisons, was performed to determine the statistical significance between individual sample groups with significance set at $p < 0.05$.

Chapter 3: Results

3.1 Nanoparticle Characterization

Image J measurements of the SEM micrographs (Figure 3.1A) of synthesized ZnO NPs showed particles of 4-6 nm in size. Observation showed the particle to be spherical in shape and uniform in size. The TiO_2 NPs, on the other hand, varied in shape and the particles had greater range in size, being 7-23 nm (Figure 3.1B).

The X-R diffractograms seen in Figure 3.1C display the characteristic ZnO peaks (JCPDS card No. 80-0075; a = 3.259Å and c = 5.209 Å). The Debye Scherrer relation indicated the crystallite size of the ZnO NPs to be 19 nm. Peaks typical of TiO_2 (JCPDS card No. 21-1272) were observed in the TIO_2 NPs as seen in Figure 3.1D. The crystallite size of these NPs was calculated to be 20nm.

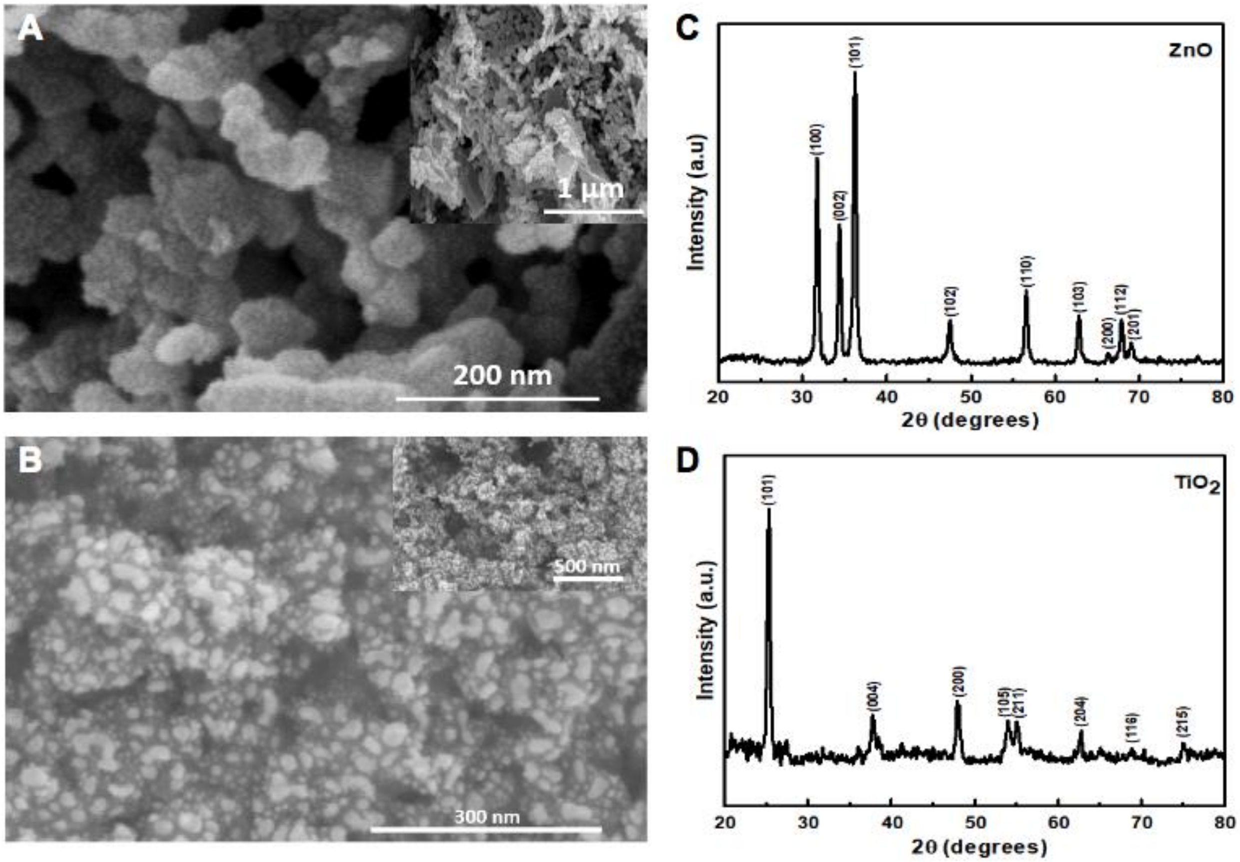

Figure 3.1: Nanoparticle Characterization. (A) SEM micrographs of ZnO NPs at different magnifications. The inset shows the low magnification image of ZnO NPs. (B) SEM micrographs of TiO_2 NPs at different magnifications. The inset shows the low magnification image of TiO_2 NP. (C) XRD patterns of ZnO NPs prepared by one pot synthesis. (D) XRD patterns of commercially procured TiO_2 NPs.

3.2 Hydroxyl Radical Generation

Confirmation of hydroxyl radical release upon UV irradiation of the NPs can be seen by analyzing fluorescence emission as seen in Figure 3.2. The addition of NPs to NaTA resulted in an emission much greater ($p < 0.001$) than when the NPs were added to DI water. Similarly, emission from 5mM NaTA also remained low. Comparing the two NP-NaTA samples, little difference (not statistically significant) was seen between the ZnO and TiO_2.

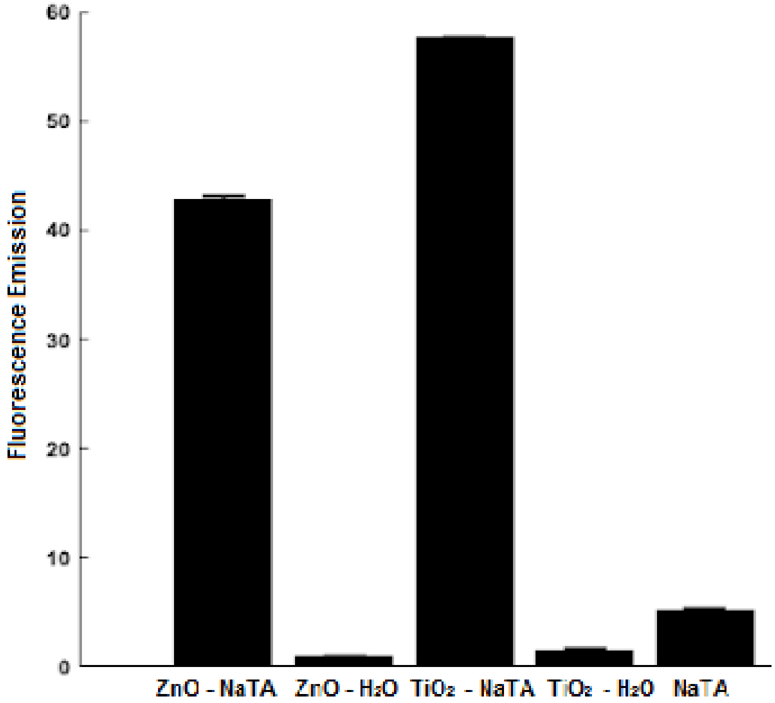

Figure 3.2: Radical Generation Probe Assay. Chart comparing fluorescence emission of ZnO and TiO_2 NPs in NaTA and DI H_2O and negative control NaTA.

3.3 Morphological Characterization of Gel Scaffolds

The two methods of production are further explained in Figure 3.3 They showed clear differences upon both gross morphological inspection (Figure 3.4) and SEM imaging (Figure 3.5) of the gels. The 3D printed gels showed the defined lines of the lattice structure (Figure 3.5A-D), while the manually cast had a smoother surface appearance (Figure 3.5E-H). SEM images of the printed structures showed smaller and better distributed pores, whereas cast gels had greater porosity and decreased uniformity in the morphology. The addition of NPs led to a significant increase in pore diameter within the 3D printed alginate group ($p < 0.002$), but not to the manually cast gel group (Figure 3.5I).

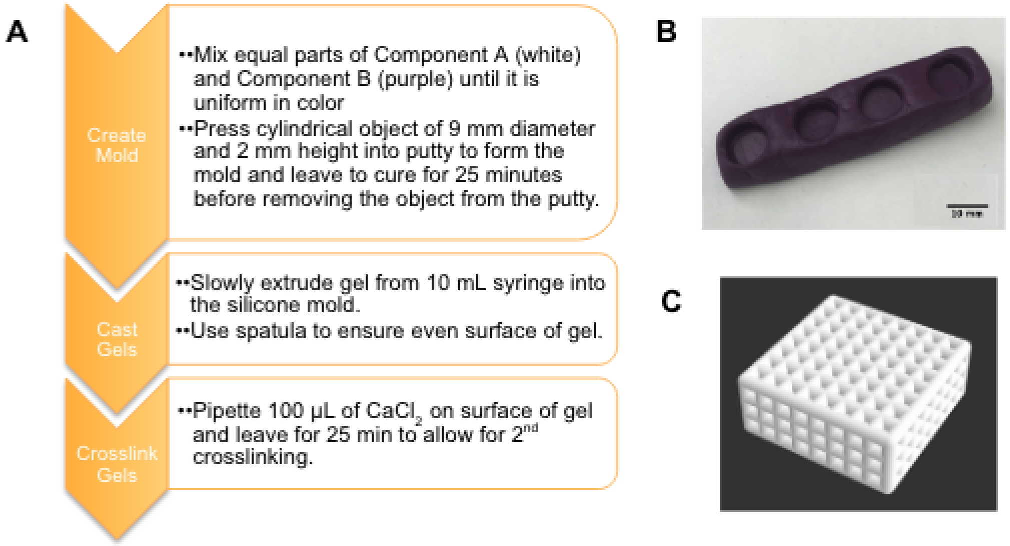

- Mix equal parts of Component A (white) and Component B (purple) until it is uniform in color
- Press cylindrical object of 9 mm diameter and 2 mm height into putty to form the mold and leave to cure for 25 minutes before removing the object from the putty.

- Slowly extrude gel from 10 mL syringe into the silicone mold.
- Use spatula to ensure even surface of gel.

- Pipette 100 µL of $CaCl_2$ on surface of gel and leave for 25 min to allow for 2nd crosslinking.

Figure 3.3: Scaffold Fabrication (A) Process for casting gels using EasyMold Silicone Putty. **(**B) Silicone mold for cast gels. (C) Lattice structure stl file image for 3D printed gel.

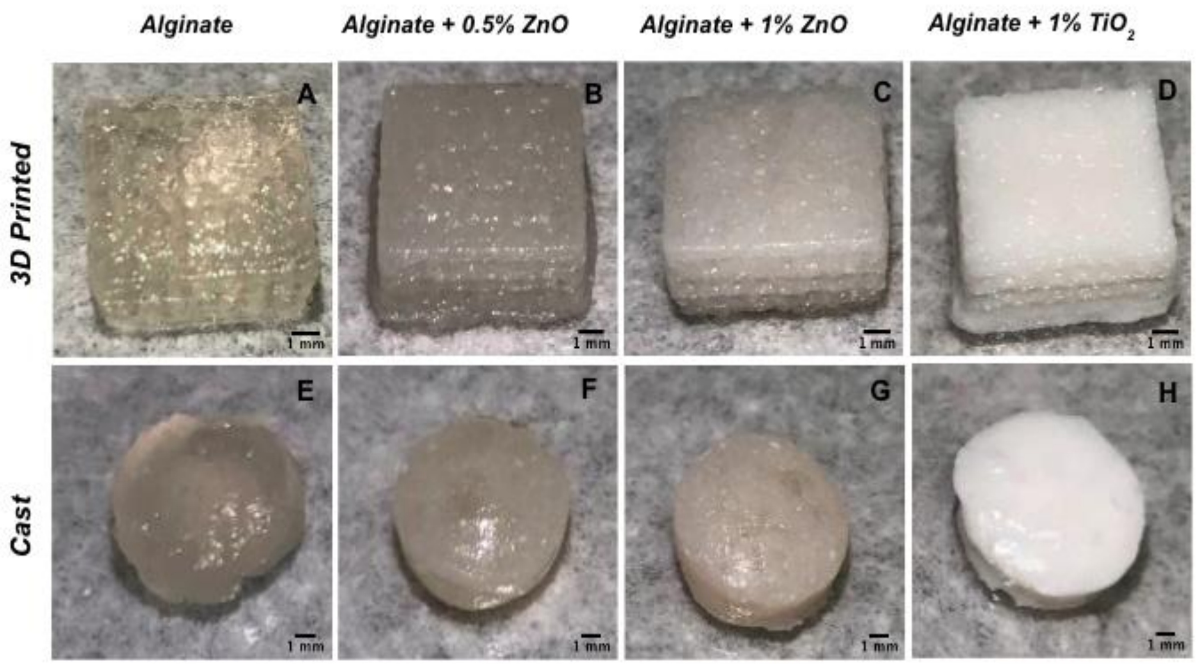

Figure 3.4: Gross Morphology (A-D) depict 3D printed lattice structures. (E-H) portray manually cast structures.

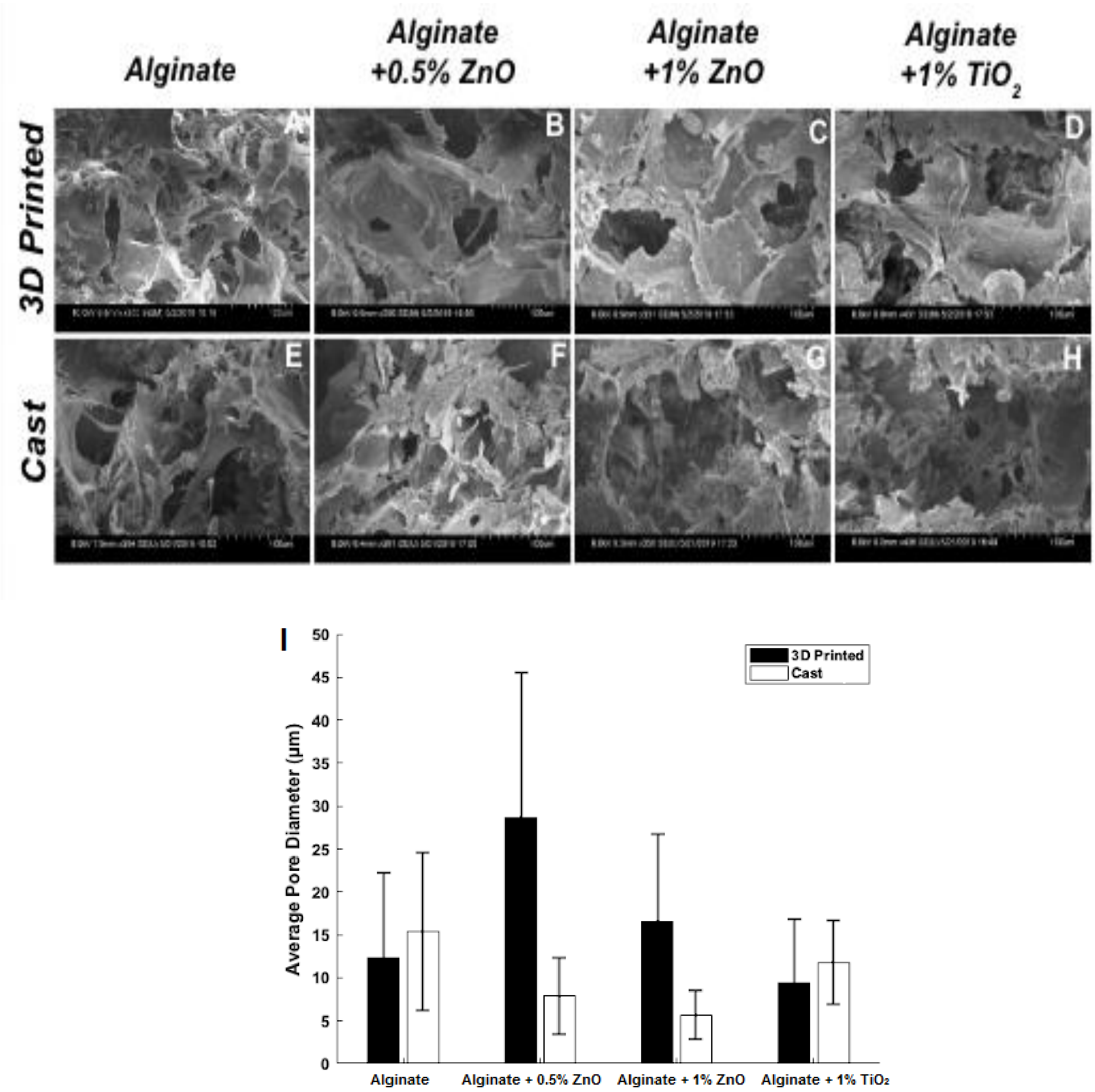

Figure 3.5: SEM Imaging and Analysis. Cross-sectional SEM imaging of (A-D) 3D printed gels and (E-H) manually cast gels. (I) Graph depicting average pore diameters of both 3D printed and manually cast gels.

XRD patterns of both the alginate only and the NP impregnated alginate can be seen in Figure 3.6. While they all retain the amorphous halo pattern common in sodium alginate [22], the alginate + ZnO gels both show the added peaks typical of ZnO NPs. The alginate + 1% ZnO shows the most prominent ZnO peaks.

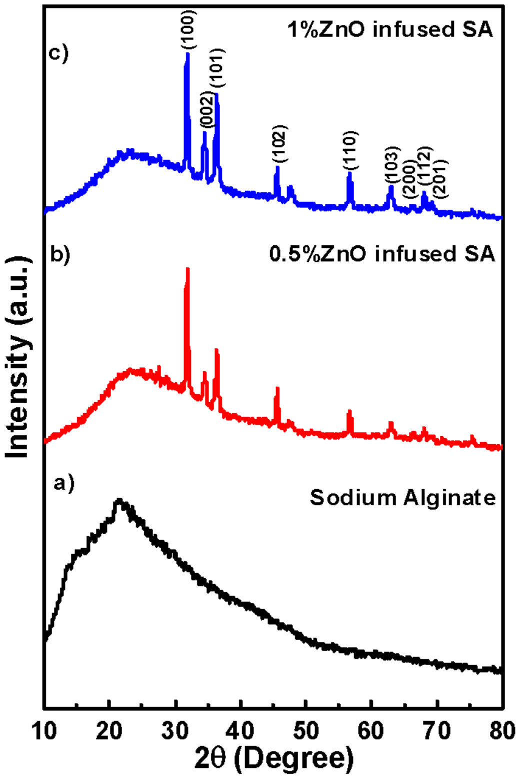

Figure 3.6: XRD patterns of a) pure sodium alginate b) 0.5% and c) 1% ZnO NP infused sodium alginate

3.4 Swelling and Degradation

The swelling behavior of the manually cast and 3D bioprinted gels over a period of 5 days was compared, as shown in Figure 3.7. Within the 3D printed group (Figure 3.7A), only TiO_2 showed significantly smaller ratio in comparison to the alginate only and 0.5% ZnO samples ($p < 0.05$). Among the manually cast sample group, however (Figure 3.7B), a significant difference was observed in swelling ratios ($p < 0.001$). This shows a more consistent pattern of swelling over a longer period of time among the 3D printed samples. Overall, the manually cast samples showed a lesser degree of swelling than those bioprinted.

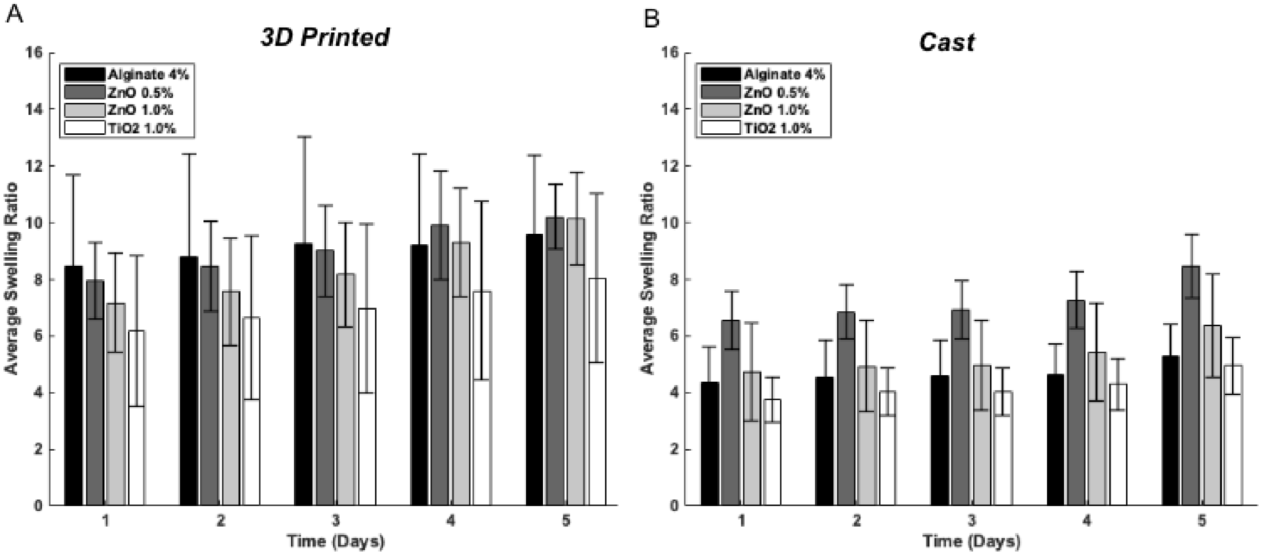

Figure 3.7: Swelling and Degradation Assay (A) Swelling analysis of 3D printed gels over a 5 day period. (B) Swelling analysis of manually cast gels over a 5 day period.

Visual tracking of the 3D printed lattice disks in PBS over 28 days can be seen in Figure 3.8. Within 7 days the alginate only samples began to lose fidelity, while TiO_2 added gels were clearly degrading. By day 28, the alginate samples were difficult to distinguish and the TiO_2 samples had disintegrated further. The alginate + ZnO samples however remained intact throughout the 28 days of observation.

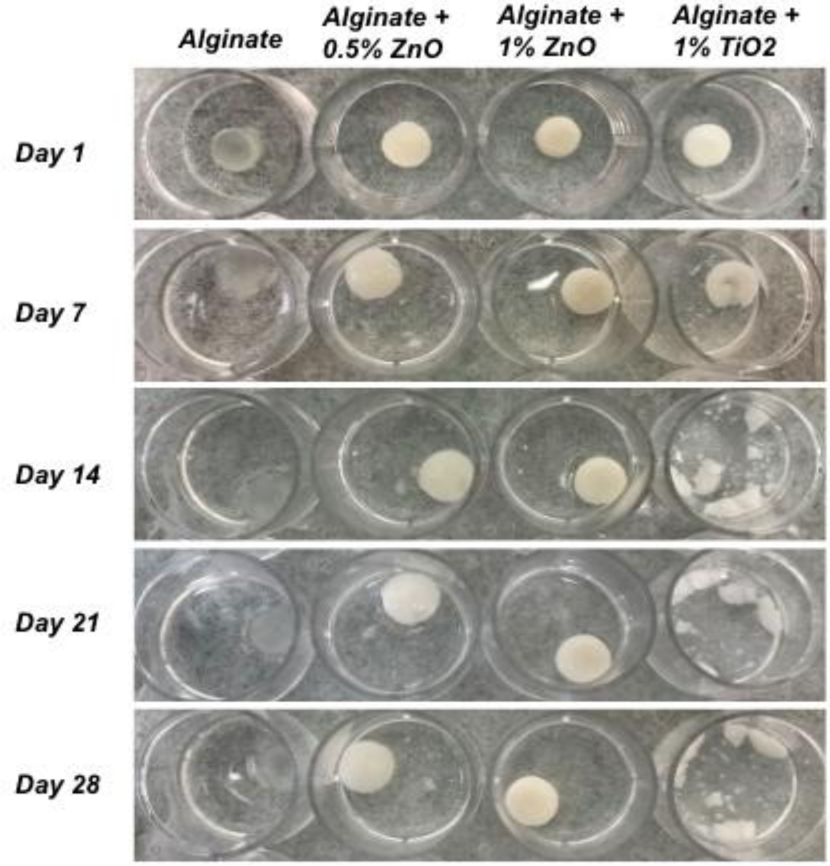

Figure 3.8: Images of samples in PBS visually tracked over time.

3.5 Mechanical Behavior

Figure 6 shows both the 3D printed and manually cast gels to have predominantly elastic behavior. Shear rheology was utilized to determine the storage and loss moduli of the samples with varying NP concentrations. A significant increase of complex viscosity ($p < 0.002$), along with storage and loss modulus ($p < 0.003$) was seen in bioprinted alginate + 1% ZnO structures (Figure 3.9A, B), Manually cast gels displayed no significant difference among samples in complex viscosity and storage and loss modulus (Figure 3.9C, D). All of the manually cast gels show greater stiffness than their 3D printed counterparts, possibly indicative of stronger crosslinking. On the other hand alginate + 1% TiO_2 seems to have no significant difference in either complex viscosity or storage and loss modulus among printed or cast gels.

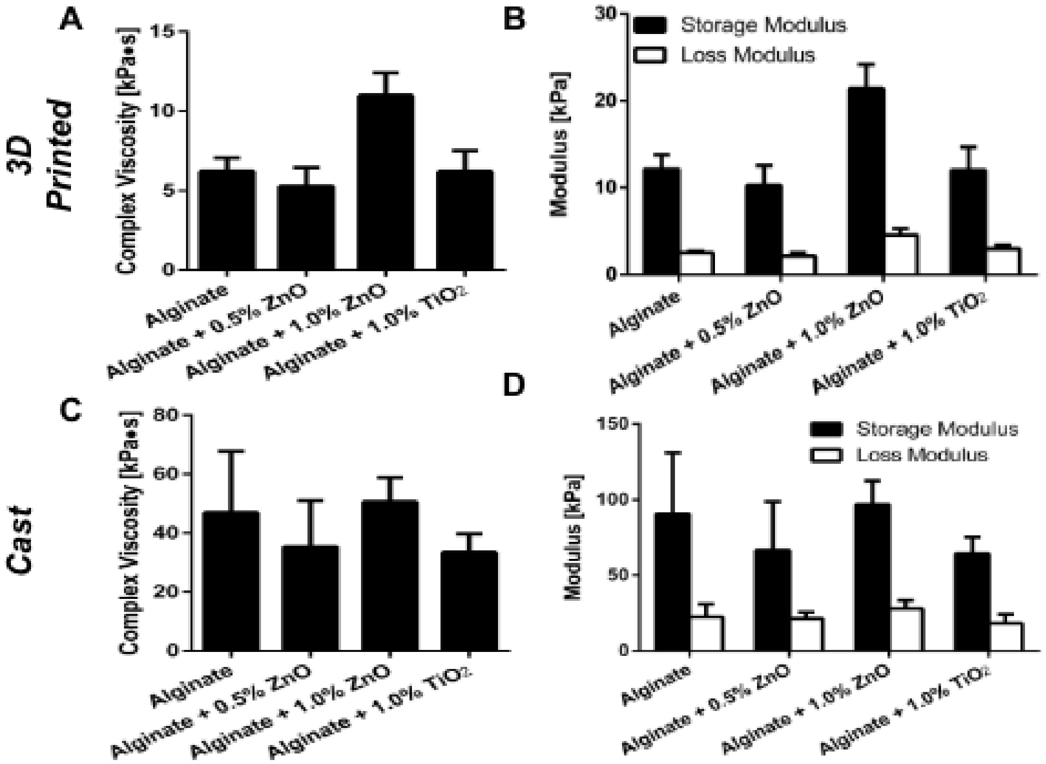

Figure 3.9: Rheological Analysis. Quantification of complex viscosity and moduli measured at 1.99 Hz of 3D Printed gels (A,B) compared to cast gels (C,D).

3.6 Humidity Retention

Figure 3.10A showcases the set up of the humidity monitoring system used to assess the moisture retention of each gel type over six days. When compared to the alginate only scaffold, alginate + 1% ZnO revealed significantly higher RH. A timeline showcasing 8-hour time points (Figure 3.10B) illustrates the alginate + 0.5% ZnO and alginate + 1% ZnO to have prolonged RH percentages with an observed difference of 11.73%. Similarly, 0.5% ZnO and 1% TiO_2 demonstrated comparable trend lines, supported by within range critical values with an observable difference of 2.49%. Quantitative analysis upon normal distribution of data, by the Kruskal-Wallis and Post-Hoc Kruskal Multiple Components tests, showed an observed difference of 31% between 1% ZnO and alginate, a difference of 25.59% between 0.5% ZnO and alginate, and a difference of 23.10% between 1% TiO_2 and alginate.

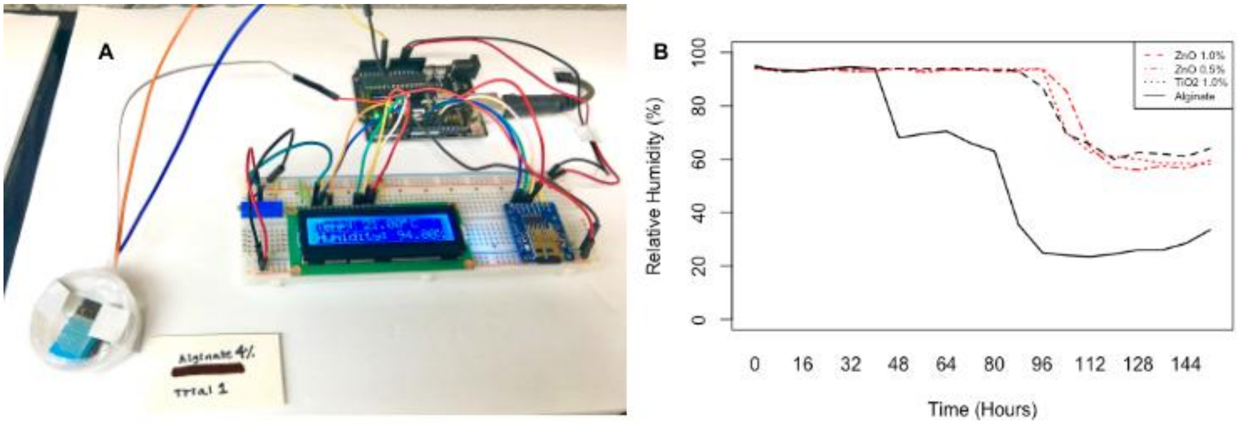

Figure 3.10: Moisture Retention Study. (A) Set up of humidity monitoring system with LCD display of RH and temperature and petri dish encased gel sample. (B) Recorded RH values displayed over 6 days in 8 hour intervals.

3.7 Bacterial Inhibition

The Kirby Bauer test as shown by Figure 3.11 showed no discernible zone of bacterial inhibition around the alginate and alginate + NP sample disks. The erythromycin disks however showed an average kill zone of 2.9-3.1 cm diameter around the *S. aureus* and 1.0-1.1 cm around the *E. coli* (Figure 3.11C,D).

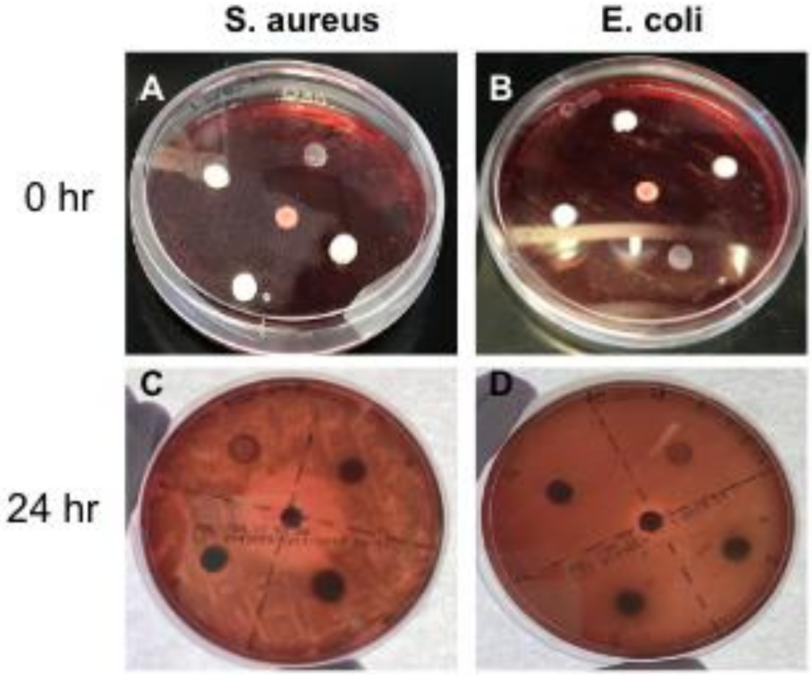

Figure 3.11: Kirby Bauer Disk Diffusion Test. (A,B) *S. aureus* and *E. coli*, respectively, streaked TSA Blood Agar plates containing sample disks before incubation. (C,D) *S. aureus* and *E. coli* plates, respectively, after 24 hours.

A bacterial broth test was set up to test the effects of both UV exposed and unexposed NP laden gels on *S. epidermidis* (Figure 3.12A). As seen in Figure 3.12B, UV exposure demonstrated a significant effect on the optical density at 600 nm (OD600). Both UV exposed and unexposed groups indicate that the addition of ZnO leads to antibacterial activity similar to that of the erythromycin control. Alternatively, the addition of TiO_2 proved to be similar to the alginate only control, with both showing much higher OD600 than the alginate + 0.5% ZnO, alginate + 1% ZnO, and erythromycin samples.

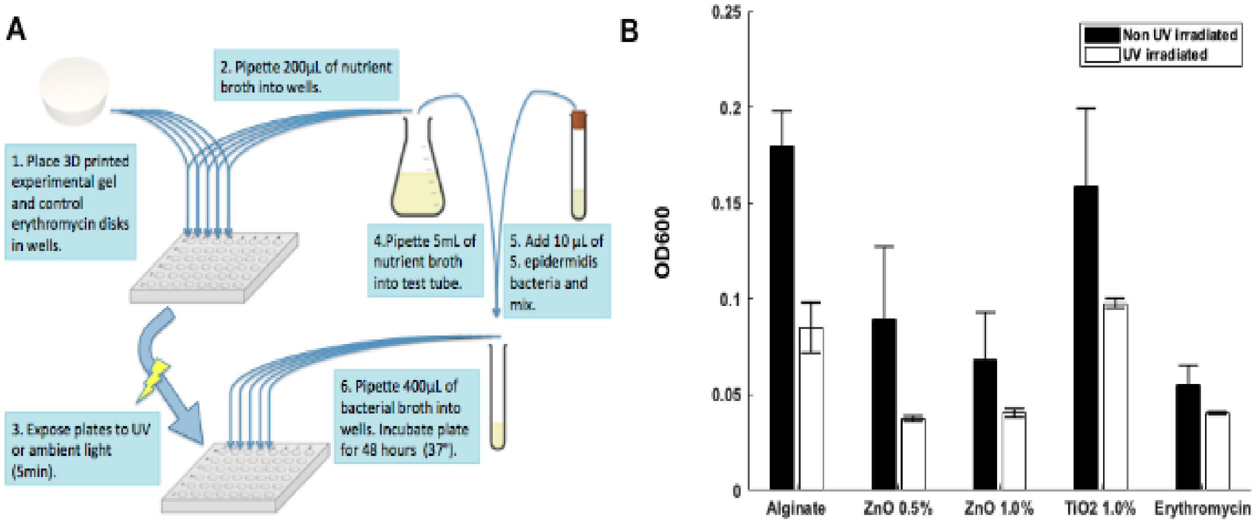

Figure 3.12: Antibacterial Testing. (A) Schematic of bacterial testing steps conducted on gels in *S. epidermidis* bacterial broth. (B) Optical density at 600nm after 48 hours of gel samples in *S. epidermidis*.

3.8 Fibroblast Compatibility

Microscopy and quantified results of cell viability are depicted in Figure 3.13. By way of visual comparison, cells retained viability in all samples, though a higher number of dead cells were existent in samples cultured in the presence of NP encapsulated alginate. Due to the homogenous distribution in the data set, transformation to normality could not be achieved, requiring independent assessment of each experimental group. This was achieved through Post-Hoc confirmation of the Kruskal Multiple Components test. The percent cell viability showed no significant difference ($p > 0.05$) between any gel samples and the control group with no gel (Figure 3.13K). No significant difference across the five groups in this study revealed uniform cell viability at 24 hr of culture. A slightly higher percentage of dead cells was observed in 0.5% ZnO. As seen in Figure 8K, 1% ZnO (88.4%) and 1% TiO_2 (93.4%) had similar percentages (5%) of live cells at identical concentrations.

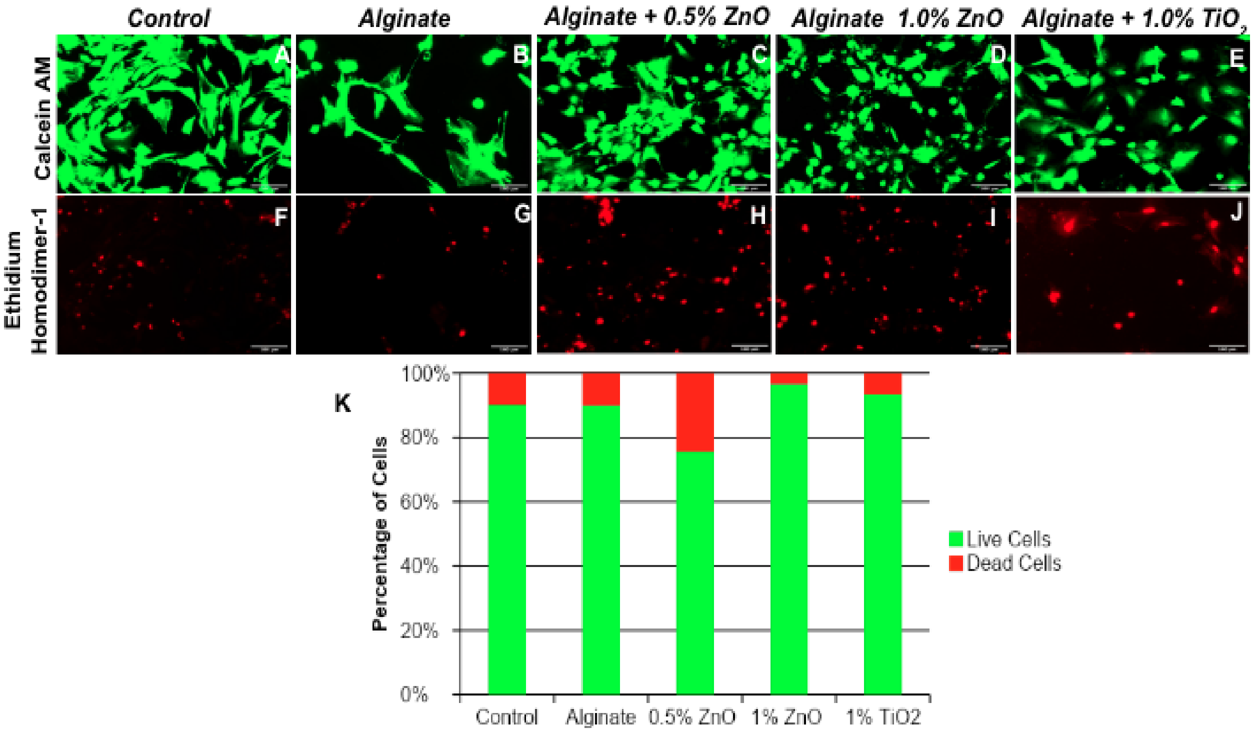

Figure 3.13: Cytocompatibility. Confocal Imaging of LIVE/DEAD Cell Viability Assay for mammalian fibroblast cells cultured with the 3D printed disks in the same wells. The images consisted of Calcein (A-E) and EtHD-1 (F-J) treated cells. Viability was quantified after a 24-hr period as a LIVE/DEAD cell percentage (K) based on particle analysis obtained through FIJI color threshold segmentation.

Chapter 4: Discussion

4.1 NP Characterization

Multiple studies have been conducted proving the characteristics of NPs, including their radical release and proposed mechanisms of action against bacteria. NPs are known to have effective interaction with biomaterials if the particle size is less than or equal to 30 nm [23]. The smaller the particles are, the larger their surface area to volume ratio. Here the particle size of the ZnO NPs is approximately 5 nm, therefore increasing the surface area available for interaction and use in medical applications [8].

As the ZnO NPs used in this study were synthesized in our lab, it was particularly essential to confirm their composition and characteristics, along with those of the commercially obtained TiO_2 that was used as a comparison. XRD helped further confirm lack of impurity in the samples.

The proposed mechanism for antibacterial defense by the NPs involves release of hydroxyl radicals to invade bacterial cells and cause their death [11]. To ensure the occurrence of this response the generation of hydroxyl radicals was confirmed by way of a terephthalic acid assay. The fluorescence seen in the NPs in NaTA guaranteed the transformation of NaTA to the fluorescent 2-hydroxyterephthalate in the presence of hydroxyl radicals [18].

4.2 NP Incorporated Gel Development

The prepared gel scaffolds had to be studied for morphological and mechanical properties to determine whether they had the characteristics necessary for wound healing applications as well. It should be noted that concentrations of 0.01-0.1% ZnO incorporation were also attempted, but exhibited insufficient radical release in preliminary testing (data not shown) and higher concentrations of 5-10% showed poor mixability due to the low density of the synthesized ZnO NPs, making for a poorly printable bioink.

The printed constructs exhibited more consistency with morphology and smaller pores compared to the cast structures. This may have to do with degree of crosslinking of the samples. The Surface Area to Volume ratio (SA:V) plays a significant role in the rate and density of crosslinking a sample. At higher SA:V ratios, crosslinking was observed to take longer to achieve complete gelation. The 3D Printed samples depict high SA and smaller V, while the reverse was true for the cast samples, more likely to demonstrate a higher V and a relatively similar SA.

Swelling studies showed a higher degree of swelling in the bioprinted gels, suggestive of a more readily available swelling capability when samples are printed, most likely attributed to its lattice structure [15]. This structure allowed for better diffusion and uptake of the solvent. In the process of wound healing, applying these characteristics will play an essential role in allowing the diffusion of nutrients and controlling any flow of wound exudates or secretions.

Degradation comparisons of the structures exhibited signs of stability and enduring fidelity in the 3D printed structure. Previous studies have shown the benefits of 3D printed in general, as well as the advantage of a lattice structure [15]. The combined effects of both calcium and zinc ions are also thought to have strengthened the crosslinking, and therefore the mechanical properties of the structure. Along with zinc’s binding site to alginate being different from that of calcium’s, zinc ions are also less selective, presumably leading to the increased crosslinking of the alginate gels in our study by the ZnO NPs [24].

This was further supported by the rheology data showing the alginate + 1% to have higher viscosity and storage and loss moduli indicating increased crosslinking effects when a higher dose of ZnO NPs was added to the alginate [24]. The cast samples having higher stiffness than those 3D printed is possibly due to the uncontrolled forming of gels onto a cast mold, resulting in disks having increased mechanical properties. In addition, the manually cast gels were solid throughout, resulting in their increased rigidity when compared to the bioprinted gels with a lattice structure. Each of these results supported the utilization of 3D printing for the manufacturing of these alginate-NP wound healing constructs.

The humidity sensor system results suggested a correlation between moisture retention and the incorporation of a larger quantity of ZnO NPs, relevant to producing a moist microenvironment favorable to healing wounds to further capitalize on the inherent properties of alginate and diminish scar tissue formation [7,25].

4.3 Cell Studies

Initial bacterial testing using the Kirby Bauer method did not show promise. It is possible that the gels were exposed to UV too long in advance before being placed on the bacteria, by which time hydroxyl radicals were no longer being released. It is also possible that the sample's surface contact with the plates was insufficient for the transfer of radicals. The zone of inhibitions shown by the erythromycin control disks served to be a proof of concept, while signaling the need to try a new method for this particular experiment. Optimizing the experiment proved to be fruitful as the bacterial broth test demonstrated bacterial growth inhibiting performance due to the ZnO NPs sample along with the erythromycin disks. The contrasting behavior by the TiO_2 samples could be attributed to their larger average size, as size is believed to affect the ability of the NPs to invade bacterial cells [26]. The comparison of UV exposed and unexposed gels also reinforced the proposed mechanism of photocatalytically activated hydroxyl radicals leading to bacterial cell death [11]. There was, however an indication of other effects at play as the ZnO scaffolds without UV exposure still showed some bacterial death. To isolate the components of the scaffold to determine their individual effects, chemical chelation can be explored in future studies. By sequestering Zn ions, a distinction could be made between the effects of Zn ions compared to those of the ROS on the *S. epidermidis*. In the case of chronic wounds, contamination by surrounding skin bacteria can occur within 48 hours [27]. *S. epidermidis* is a bacterium commonly found on the skin, making it a likely cause of infection and primary target in this study [28].

Studies have shown correlation of lower concentration of ZnO NPs to increased cell viability [20]. By showing no significant difference in cell viability among samples, the implications of our study remain that the ZnO NPs toxicity lies below the threshold for substantial cell damage. The higher percentage of dead cells seen in alginate + 0.5 % than in alginate + 1% ZnO or TiO_2 indicates the influence of NP dispersion on cell viability. The cells used, MITC-STO, were generated from mouse embryonic fibroblasts and treated with Mitomycin C to inhibit replication. Fibroblasts are commonly found in the skin and an important component in wound healing. Further studies with varying NP concentrations should be considered to assess any correlation between cell death and concentration and better determine the optimal balance between bacterial cell death and fibroblast cell proliferation.

Chapter 5: Conclusion

This study sought to develop a hydrogel that confirms the antibacterial properties of ZnO NPs in an effort to utilize 3D printing with such a material for increased healing in chronic wounds. The easy to formulate gel was formed through manual casts and 3D printed scaffolds that were used for their comparative characteristics. The study saw the use of compositional, mechanical, and structural analyses to discover the behaviors of the gel as an agent for the ZnO NPs. Furthermore, results involving *in vitro* studies demonstrate the potential our gel would have to address chronic wounds in patients.

The NP composition and the formation of hydroxyl radicals by the combustion synthesized ZnO was confirmed. In addition, the developed gels' compositions were confirmed to be of alginate and ZnO or TiO_2 NPs by SEM and XRD experiments. Swelling, degradation and humidity studies showed the printed alginate + ZnO NP gels to have an enhanced structure and retention of moisture suitable for wound healing.

The alginate and ZnO mixture demonstrated promise on biocompatibility as *in vitro* testing using fibroblasts saw no significant damage to cells while broth optical density showed its ability to kill bacteria. Across the board, this study gives insight into the ability to produce ZnO-alginate gels capable of eliminating bacteria and allowing cell viability, all while being structurally and mechanically durable to maintain a chronic wound.

5.1 Future work

Future work on this study could involve the incorporation of the ZnO NPs in various printable bioink blends such as alginate-gelatin or alginate-collagen. This would allow us to exploit the different properties of multiple hydrogel composites which have been studied for these applications [29,30]. Doing so would allow for greater levels of material manipulation as the optimal structure for healing of any tissue is sought.

Another possibility includes optimizing the Ca^{2+} or Zn^{2+} ion crosslinking of alginate by changing time of exposure and amount of crosslinker in order to determine the effect of varying elastic modulus on cell proliferation during wound healing. Substrate stiffness has been shown to have an effect on fibroblast proliferation [31]. Further effort should hence be placed into understanding the physical forces that could potentially speed up the wound healing process.

A third suggestion that could be performed for the continuation of this study includes further testing on a wider range of common wound pathogens adding bacteria such as *Pseudomonas aeruginosa*, as well as *Candida albicans* for the exploration of antifungal properties [32]. Such studies would provide insight on the range of issues the Alginate-ZnO gel mixture could help remedy, making our gel a more versatile product.

References

1. O'Brien, F. J. Biomaterials & scaffolds for tissue engineering. *Mater. Today* **14**, 88–95 (2011).
2. Seliktar, D. *Designing Cell-Compatible Hydrogels for Biomedical Applications*.
3. Drury, J. L. & Mooney, D. J. Hydrogels for tissue engineering: Scaffold design variables and applications. *Biomaterials* **24**, 4337–4351 (2003).
4. Peiró, C. *et al.* Inflammation, glucose, and vascular cell damage: The role of the pentose phosphate pathway. *Cardiovasc. Diabetol.* **15**, (2016).
5. Ousey, K., Cutting, K. F., Rogers, A. . & Rippon, M. G. The Importance of Hydration in Wound Healing: Reinvigorating the Clinical Perspective. **25**, 124–130 (2016).
6. Menke, N. B., Ward, K. R., Witten, T. M., Bonchev, D. G. & Diegelmann, R. F. Impaired wound healing. *Clin. Dermatol.* **25**, 19–25 (2007).
7. Paul, W. & Sharma, C. P. *Chitosan and Alginate Wound Dressings: A Short Review*. *Trends Biomater. Artif. Organs* **18**, (2004).
8. Mihai, M. M., Dima, M. B., Dima, B. & Holban, A. M. Nanomaterials for wound healing and infection control. *Materials* **12**, (2019).
9. Tan, S. T. & Dosan, R. Lessons From Epithelialization: The Reason Behind Moist Wound Environment. *Open Dermatol. J.* **13**, 34–40 (2019).
10. Aderibigbe, B. A. & Buyana, B. Alginate in wound dressings. *Pharmaceutics* **10**, (2018).
11. Siddiqi, K. S., ur Rahman, A., Tajuddin & Husen, A. Properties of Zinc Oxide Nanoparticles and Their Activity Against Microbes. *Nanoscale Research Letters* **13**, (2018).
12. Zan, L., Fa, W., Peng, T. & Gong, Z. kui. Photocatalysis effect of nanometer TiO2 and

TiO2-coated ceramic plate on Hepatitis B virus. *J. Photochem. Photobiol. B Biol.* **86**, 165–169 (2007).

13. Duty, C. *et al.* What makes a material printable? A viscoelastic model for extrusion-based 3D printing of polymers. *J. Manuf. Process.* (2018). doi:10.1016/j.jmapro.2018.08.008
14. Guvendiren, M., Molde, J., Soares, R. M. D. & Kohn, J. Designing Biomaterials for 3D Printing. *ACS Biomaterials Science and Engineering* **2**, 1679–1693 (2016).
15. Anil Kumar, S. *et al.* A Comparative Study of a 3D Bioprinted Gelatin-Based Lattice and Rectangular-Sheet Structures. *Gels* **4**, 73 (2018).
16. Islam, M. T. *et al.* Sucrose-Mediated Fast Synthesis of Zinc Oxide Nanoparticles for the Photocatalytic Degradation of Organic Pollutants in Water. *ACS Omega* **4**, 6560–6572 (2019).
17. Zade, V., Mallesham, B., Shantha-Kumar, S., Bronson, A. & Ramana, C. V. Interplay between Solubility Limit, Structure, and Optical Properties of Tungsten-Doped Ga 2 O 3 Compounds Synthesized by a Two-Step Calcination Process. *Inorg. Chem.* **58**, 3707–3716 (2019).
18. Nosaka, Y., Komori, S., Yawata, K., Hirakawa, T. & Nosaka, A. Y. Photocatalytic •OH radical formation in TiO2 aqueous suspension studied by several detection methods. *Phys. Chem. Chem. Phys.* **5**, 4731–4735 (2003).
19. Al-Twood, A. I. Calcium alginate dressing accelerates split skin graft donor site healing. *Br. J. Plast. Surg.* **42**, (1989).
20. Mohandas, A., Sudheesh Kumar, P. T., Raja, B., Lakshmanan, V. K. & Jayakumar, R. Exploration of alginate hydrogel/nano zinc oxide composite bandages for infected wounds. *Int. J. Nanomedicine* **10**, 53–56 (2015).

21. Joddar, B., Garcia, E., Casas, A. & Stewart, C. M. Development of functionalized multi-walled carbon-nanotube-based alginate hydrogels for enabling biomimetic technologies. *Sci. Rep.* **6**, (2016).

22. Finotelli, P. V, Sampaio, D. A., Morales, M. A., Rossi, A. M. & Rocha-Leão, M. H. Ca ALGINATE AS SCAFFOLD FOR IRON OXIDE NANOPARTICLES SYNTHESIS. **25**, 759–764

23. Sirelkhatim, A. *et al.* Review on zinc oxide nanoparticles: Antibacterial activity and toxicity mechanism. *Nano-Micro Letters* **7**, 219–242 (2015).

24. Chan, L. W., Jin, Y. & Heng, P. W. S. *Cross-linking mechanisms of calcium and zinc in production of alginate microspheres*. *International Journal of Pharmaceutics* **242**, (2002).

25. Junker, J. P. E., Kamel, R. A., Caterson, E. J. & Eriksson, E. Clinical Impact Upon Wound Healing and Inflammation in Moist, Wet, and Dry Environments. *Adv. Wound Care* **2**, 348–356 (2013).

26. Xie, Y., He, Y., Irwin, P. L., Jin, T. & Shi, X. Antibacterial activity and mechanism of action of zinc oxide nanoparticles against Campylobacter jejuni. *Appl. Environ. Microbiol.* **77**, 2325–2331 (2011).

27. Mustoe, T. A., O'Shaughnessy, K. & Kloeters, O. Chronic wound pathogenesis and current treatment strategies: A unifying hypothesis. *Plastic and Reconstructive Surgery* **117**, (2006).

28. von Eiff, C., Heilmann, C. & Peters, G. *Staphylococcus epidermidis: Why is it so successful?* (1998).

29. Boateng, J., Burgos-Amador, R., Okeke, O. & Pawar, H. Composite alginate and gelatin based bio-polymeric wafers containing silver sulfadiazine for wound healing. *Int. J. Biol.*

Macromol. **79**, 63–71 (2015).

30. Xie, H. *et al.* Preparation of chitosan-collagen-alginate composite dressing and its promoting effects on wound healing. *Int. J. Biol. Macromol.* **107**, 93–104 (2018).
31. Hopp, I. *et al.* The influence of substrate stiffness gradients on primary human dermal fibroblasts. *Biomaterials* **34**, 5070–5077 (2013).
32. Negut, I., Grumezescu, V. & Grumezescu, A. M. Treatment strategies for infected wounds. *Molecules* **23**, (2018).

Curriculum Vita

Carol Cleetus was born and raised in El Paso, TX. She graduated from Maxine L. Silva Health Magnet High School and continued her education at the University of Texas as El Paso (UTEP). From UTEP she obtained her Bachelor of Science in Biological Sciences with a Biomedical Concentration. Carol went on to pursue graduate education, receiving her Master of Science in Biomedical Engineering from UTEP in May 2020.

During her time at UTEP, Carol was a graduate research assistant in the Inspired Materials and Stem Cell Based Tissue Engineering Laboratory (IMSTEL). In IMSTEL, she worked under Binata Joddar, Ph.D. to study the characteristics of zinc oxide nanoparticles and alginate scaffolds. This allowed for exploration of potential for these material composites in wound healing applications. She was also involved in animal research, investigating the effects of a cryo-induced myocardial infarction in a rat model in an effort to study cardiac disease and tissue engineering. These works have been submitted for publication and Carol plans to continue with a career in research in an effort to make further contributions in the field of biomedical engineering.